

Spectral Response Function-Guided Deep Optimization-Driven Network for Spectral Super-Resolution

Jiang He^{ID}, Jie Li^{ID}, Member, IEEE, Qiangqiang Yuan^{ID}, Member, IEEE,
Huanfeng Shen^{ID}, Senior Member, IEEE, and Liangpei Zhang^{ID}, Fellow, IEEE

Abstract—Hyperspectral images (HSIs) are crucial for many research works. Spectral super-resolution (SSR) is a method used to obtain high-spatial-resolution (HR) HSIs from HR multispectral images. Traditional SSR methods include model-driven algorithms and deep learning. By unfolding a variational method, this article proposes an optimization-driven convolutional neural network (CNN) with a deep spatial-spectral prior, resulting in physically interpretable networks. Unlike the fully data-driven CNN, auxiliary spectral response function (SRF) is utilized to guide CNNs to group the bands with spectral relevance. In addition, the channel attention module (CAM) and the reformulated spectral angle mapper loss function are applied to achieve an effective reconstruction model. Finally, experiments on two types of data sets, including natural and remote sensing images, demonstrate the spectral enhancement effect of the proposed method, and also, the classification results on the remote sensing data set verified the validity of the information enhanced by the proposed method.

Index Terms—Convolutional neural network (CNN), hyperspectral image (HSI), optimization driven, spectral response function (SRF), spectral super-resolution (SSR).

I. INTRODUCTION

HYPERSPECTRAL (HS) imaging is a technique used to explore the spectral characteristics of objects completely via the fine resolution of scene radiance. Hyperspectral images (HSIs) processing, such as segmentation [1], classification [2], detection [3], [4], and tracking [5], have gained increasing attention due to the rich spectral information. HS imaging has also been developed for numerous applications ranging from remote sensing [6]–[8] to medical imaging [9].

Manuscript received 3 February 2020; revised 16 August 2020 and 8 December 2020; accepted 26 January 2021. Date of publication 18 February 2021; date of current version 2 September 2022. This work was supported in part by the National Natural Science Foundation of China under Grant 41922008, Grant 62071341, and Grant 61971319; in part by the Hubei Science Foundation for Distinguished Young Scholars under Grant 2020CFA051; and in part by the Fundamental Research Funds for the Central Universities under Grant 531118010209. (Corresponding authors: Jie Li; Qiangqiang Yuan.)

Jiang He, Jie Li, and Qiangqiang Yuan are with the School of Geodesy and Geomatics, Wuhan University, Wuhan 430079, China (e-mail: jiang_he@whu.edu.cn; jli89@sgg.whu.edu.cn; yqiang86@gmail.com).

Huanfeng Shen is with the School of Resource and Environmental Sciences, Wuhan University, Wuhan 430079, China (e-mail: shenhf@whu.edu.cn).

Liangpei Zhang is with the State Key Laboratory of Information Engineering in Surveying, Mapping, and Remote Sensing, Wuhan University, Wuhan 430079, China (e-mail: zlp62@whu.edu.cn).

This article has supplementary material provided by the authors and color versions of one or more figures available at <https://doi.org/10.1109/TNNLS.2021.3056181>.

Digital Object Identifier 10.1109/TNNLS.2021.3056181

HS sensors acquire scene radiance with numerous spectral bands in a fine wavelength range. However, less energy radiance is sensed by each detector element when the spectral resolution is high. The sensors require a long exposure time to obtain an acceptable signal-to-noise-ratio of each band. Compared with red-green-blue (RGB) and multispectral images (MSIs), HSIs always lack fine spatial resolution. This limitation affects the availability of HSIs for applications that require high spatial resolution (HR). Many researchers have proposed the direct reconstruction of HR HSIs by image super-resolution (SR) of low-spatial-resolution (LR) HSIs to enhance the spatial details of HSIs. Akgun *et al.* [10] proposed a model that can represent the HS observations as weighted linear combinations and used a set-theoretic method as a solution. Gu *et al.* [11] proposed an SR algorithm that uses an indirect approach based on spectral unmixing and designed learning-based SR mapping as the backpropagation neural network. The aforementioned methods only utilize LR HSIs to reconstruct HR HSIs. However, poor spatial enhancement is observed when the ratio between LR and HR is large.

With the development of detector elements, abundant sensors are currently designed to achieve a good representation of spatial details and temporal variations. However, these sensors capture only three or four spectral bands for a very HR (≤ 10 m), especially for remote sensing satellites, such as Sentinel-2, GaoFen-2, QuickBird, and WorldView. Although MSIs generally have an HR, they cannot completely represent the spectral characteristics of the object by using only a few spectral channels.

Combining the respective advantages of HSIs and MSIs, some researchers use HR MSIs as auxiliary data to improve the spatial resolution of HSIs. Hardie *et al.* [12] presented a novel maximum *a posteriori* (MAP) estimator for enhancing the spatial resolution. The MAP estimator used a spatially varying statistical model based on vector quantization to exploit localized correlations. Kawakami *et al.* [13] fused HSIs with images from RGB cameras by initially applying an unmixing algorithm to the HS input and then regarding the unmixing problem as the search for input factorization. Akhtar *et al.* [14] proposed a fusion algorithm of MSIs and HSIs using nonparametric Bayesian sparse representation. Meng *et al.* [15] proposed an integrated relationship model that relates to the HSIs and multisource HR observations based on the MAP framework. Palsson *et al.* [16] proposed

a novel method for the fusion of MSIs and HSIs, which is performed in the low-dimensional PC subspace; thus, only the first few PCs must be estimated instead of all spectral bands. The fusion-based method can substantially improve the spatial resolution of the image through the HR spatial detail injection. However, the HR MSIs corresponding to the LR HSIs covering the same area and acquired at a similar time are not always easily accessible in many cases. Although HR MSI data were available, the registration and preprocessing of multisensor data are difficult. Besides, this difficulty affects the accuracy and performance of algorithms.

The spectral super-resolution (SSR) methods are proposed to overcome the unavailability of HRHS images by increasing the spectral resolution of MS images without auxiliary HS images, which focuses on the spectral transformation rather than the spatial resolution enhancement. In 2008, Parmar *et al.* [17] first reconstructed HS image from RGB image by sparse recovery. Inspired by this research, Arad and Ben-Shahar [18] proposed the computation of the dictionary representation of each RGB pixel by using the orthogonal match pursuit algorithm. Wu *et al.* [19] substantially improved Arad's method by pretraining an overcomplete dictionary as anchor points to perform a nearest neighbor search based on the A+ algorithm proposed by Timofte *et al.* [20] from spatial SR. In 2018, Akhtar and Mian [21] modeled natural spectra under Gaussian processes and combined them with RGB images to recover HS images. Without dictionary learning, Nguyen *et al.* [22] explored a strategy to train a radial basis function network that presents the spectral transformation to recover the scene reflectance using training images. Deep learning, especially convolutional neural network (CNN), has recently attracted increasing attention and has been demonstrated to outperform most traditional approaches in areas, such as segmentation [23], classification [24], denoising [25], and spatial SR [26]. Inspired by the semantic segmentation architecture *Tiramisu* [27], Galliani *et al.* [28] proposed *DenseUnet* with 56 convolutional layers to show good performance. To prove that comparable performance can be achieved by shallow learning, Can *et al.* [29] proposed a moderately deep residual CNN to recover spectral information of RGB images. Shi *et al.* [30] designed a deep CNN with dense blocks and a novel fusion scheme to deal with the situation when the spectral response function (SRF) is unknown. Optimizing bands pixel-by-pixel, Gewali *et al.* [31] proposed a deep residual CNN to learn both the optimized MS bands and the transformation to reconstruct HS spectra from MS signals. Arun *et al.* [32] explored a CNN-based encoding-decoding architecture to model the spatial-spectral prior to improve recovery. However, the deep learning-based model is similar to a data-driven black box with the ideal capability of feature learning and nonlinear mapping. Recently, interpretability specific to the problem has been identified as an important part of CNN development. Some research works have attempted to achieve this purpose. Most of them are trying to combine deep learning with physical model-driven methods. By learning a regularization term for the variational model or MAP framework, CNNs are utilized to achieve some physical mappings as approximate operator and

denoiser in many image processing tasks, such as denoising [33], [34], compressive sensing [35], data fusion [36], and deblurring [37]. However, these methods just utilized the pre-trained CNN prior but did not update it in model-driven optimization. Also, the training of those algorithms is broken into two stages: learning optimization and variational optimization, which is difficult to inherit the data-driven advantages of deep learning.

In this article, an end-to-end optimization-driven CNN with the spectral degradation model is built and different spectral ranges are grouped to be reconstructed based on SRFs. The SRF is utilized to guide the CNN group in the spectral similar bands to further enhance spectral information. Rather than alternately running a variational model and CNN, an optimization-driven CNN with deep spatial-spectral prior and parametric self-learning is proposed. The proposed CNN repeatedly updates the intermediate HS image in an end-to-end manner. The contributions are as follows.

- 1) An end-to-end optimization-driven CNN is proposed by combining the data-driven method with the optimization algorithm to improve the model interpretability. The channel attention module (CAM) is introduced in the proposed model to embed the parameter self-learning considering spectral differences of bands into CNN.
- 2) The SRF is employed as a guide to aid CNN in grouping suitable spectral bands to reconstruct HS information and learn good spectral details from the true spectral channel ranges in the proposed CNN.
- 3) The spatial-spectral convolutional layers are used to model deep spatial-spectral prior. Also, the proposed network employed a fast spatial-spectral loss function reformulated from L1 and spectral angle mapper (SAM) losses to reach quick convergence and good spatial-spectral constraints.

The remaining part of this article is organized as follows. Section II describes the degradation model and derives the SSR algorithm based on the variational model to the proposed optimization-driven CNN. Section III presents the experiments on two types of data sets, including five data sets from natural to remote sensing images, and some discussions of deep learning-based methods are also made. Finally, we draw some conclusions in Section IV.

II. PROPOSED METHOD

First, the spectral degradation between MS and HS imaging is modeled in this section. Based on this model, the SSR problem is formulated and split into two subproblems. Finally, by learning physical mappings using CNNs, the proposed SSR network with a joint spatial-spectral HSI prior (HSRnet) is comprehensively demonstrated. The framework of the proposed method is shown in Fig. 1. The proposed framework can be divided into two parts, including an initial restoration network and optimization stages with attention-based parametric self-learning and spatial-spectral networks (SSNs), which followed the data flow in model-based methods.

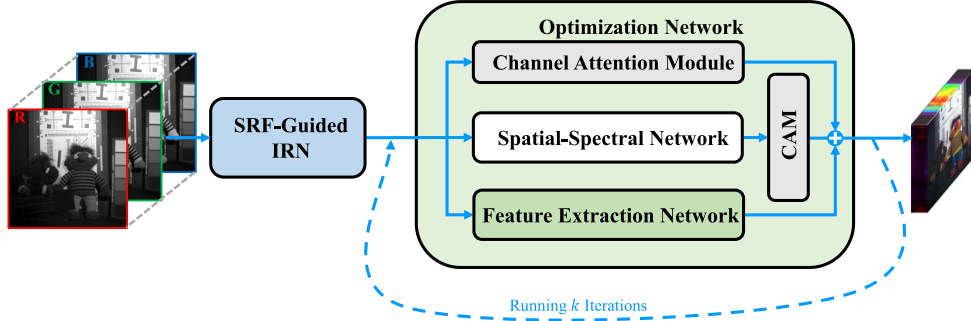


Fig. 1. Framework of the proposed HSRnet.

A. Model Formulation

Let $\mathbf{X} \in R^{W \times H \times C}$ represent the observed HSI, where C is the number of the spectral channels and W and H are the width and height, respectively, and $\mathbf{Y} \in R^{W \times H \times c}$ represent the observed MSI, where $c < C$ is the number of multispectral bands, specifically for RGB image, with $c = 3$. Varying in SRF, the sensors obtain different MS or HS data with different bands. A transformation matrix $\Phi \in R^{c \times C}$ can be used to describe the spectral degradation between MS and HS imaging as follows:

$$\mathbf{Y} = \Phi \mathbf{X}. \quad (1)$$

The spectral transform matrix is closely related to SRF, which can be approximately estimated by some methods, such as Hysure [38] and RWL1-SF [39]. According to (1), the relationship between MSIs and HSIs is illuminated. However, in SSR, obtaining a high-dimensional cube from low-dimensional data is an underdetermined problem. The high-dimensional HSIs can be approximately predicted by adopting some priors to a minimization problem to constrain the solution space as follows:

$$\hat{\mathbf{X}} = \arg \min_{\mathbf{X}} \|\mathbf{Y} - \Phi \mathbf{X}\|^2 + \gamma \mathcal{R}(\mathbf{X}) \quad (2)$$

where γ is a tradeoff parameter and $\mathcal{R}(\cdot)$ is a regularization function. As in (2), the minimization problem is constrained by two parts. The first term is the data fidelity term that limits the solution according to the degradation model, and the second regularization term constrains the predicted $\hat{\mathbf{X}}$ with an HSI prior.

The variable splitting technique can be employed to further solve this minimization problem and separate the two terms in (2). An auxiliary variable \mathbf{H} is introduced to reformulate (2) to obtain a constrained optimization problem, which is shown as follows:

$$\hat{\mathbf{X}} = \arg \min_{\mathbf{X}} \|\mathbf{Y} - \Phi \mathbf{X}\|^2 + \gamma \mathcal{R}(\mathbf{H}), \quad \text{s.t. } \mathbf{H} = \mathbf{X}. \quad (3)$$

According to the half-quadratic splitting method, the cost function is then transformed into

$$L(\hat{\mathbf{X}}, \hat{\mathbf{H}}) = \|\mathbf{Y} - \Phi \mathbf{X}\|^2 + \mu \|\mathbf{H} - \mathbf{X}\|^2 + \gamma \mathcal{R}(\mathbf{H}) \quad (4)$$

where μ is a penalty parameter with various values in different iterations. Using the variable splitting technique, (4) can be

resolved by solving two subproblems iteratively as

$$\hat{\mathbf{X}}^{k+1} = \arg \min_{\mathbf{X}} \|\mathbf{Y} - \Phi \mathbf{X}\|^2 + \mu \|\mathbf{H}^k - \mathbf{X}\|^2 \quad (5)$$

$$\hat{\mathbf{H}}^{k+1} = \arg \min_{\mathbf{H}} \|\mathbf{H} - \mathbf{X}^{k+1}\|^2 + \lambda \mathcal{R}(\mathbf{H}) \quad (6)$$

where $\lambda = \gamma/\mu$ is another penalty parameter related to μ and γ . The degradation model Φ and HSI prior $R(\mathbf{H})$ can be considered individually due to the variable splitting technique.

Considering the \mathbf{X} -subproblem, instead of directly solving the \mathbf{X} -subproblem as a least-squares problem, an approximate solution updated by the gradient descent algorithm is employed in this article as follows:

$$\begin{aligned} \hat{\mathbf{X}}^{k+1} &= \mathbf{X}^k - \varepsilon [\Phi^T (\Phi \mathbf{X}^k - \mathbf{Y}) + \mu (\mathbf{X}^k - \mathbf{H}^k)] \\ &= [(1 - \varepsilon \mu) \mathbf{I} - \varepsilon \Phi^T \Phi] \mathbf{X}^k + \varepsilon \Phi^T \mathbf{Y} + \varepsilon \mu \mathbf{H}^k. \end{aligned} \quad (7)$$

As described in [33], the \mathbf{H} -subproblem in (6) can be rewritten as

$$\hat{\mathbf{H}}^{k+1} = \arg \min_{\mathbf{H}} \frac{1}{2(\sqrt{\lambda/2})^2} \|\mathbf{H} - \mathbf{X}^{k+1}\|^2 + \mathcal{R}(\mathbf{H}). \quad (8)$$

Equation (8) can be regarded as denoising (both in spatial and spectral domain) images with the noise level of $\sqrt{\lambda}/2$ with the constraint of HSI priors. Also, the prior includes two meanings: one is the restraint on spatial information, for example, clearer edges, texture features, local smoothness, nonlocal self-similarity, and non-Gaussianity; the other is the restraint on spectral information, such as sparsity and high correlations between spectra. Unlike the total variation or sparsity prior, the HSI prior contains more than one property, which should be modeled with nonlinearity to increase the accuracy [33].

With good nonlinear learning ability, deep learning-based methods are proved to be capable of many image restoration tasks. In this article, an SSN is proposed to achieve the optimization as (8) describes because of the nonlinearity of HSI prior. By extracting spatial and spectral information, the intermediate results are updated following the constraint of (6). Thus, the optimization of \mathbf{H} is rewritten as

$$\hat{\mathbf{H}}^{k+1} = \text{Spa_Spec}(\mathbf{X}^k) \quad (9)$$

where $\text{Spa_Spec}(\cdot)$ presents the SSN. The details will be described in Section II-B. With a new way of updating \mathbf{H} , the original optimization method, which alternatively updates \mathbf{H} and \mathbf{X} until convergence, can be rewritten to a unified

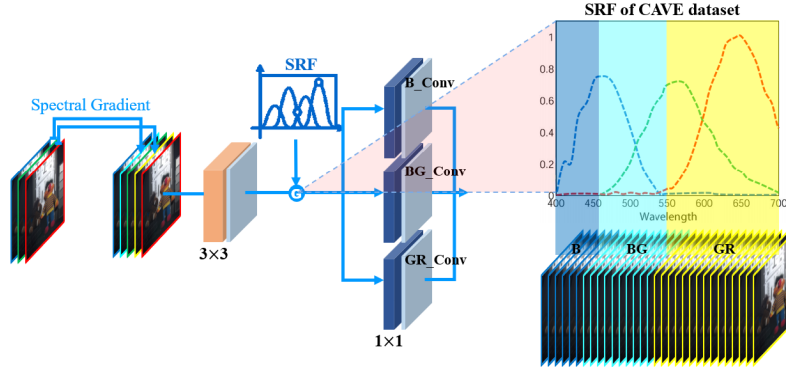


Fig. 2. IRN block.

updating of X . Considering (7) and (9), reformulated optimization is as follows:

$$\hat{X}^{k+1} = \bar{\Phi}^T Y + \varepsilon \Phi^T Y + \varepsilon \mu \cdot \text{Spa_Spec}(X^k) \quad (10)$$

where $\bar{\Phi} = (1 - \varepsilon \mu)I - \varepsilon \Phi^T \Phi$ indicates a new transformation matrix to the intermediately reconstructed image X^k .

With the help of the gradient descent algorithm and the HSI prior, the proposed method is to update the intermediate X^k with a linear combination of three parts, including the initial restoration $\Phi^T Y$, the transformed X^k , and the spatial-spectral prior to X^k . The initial restoration $\Phi^T Y$ and $\bar{\Phi}$ and parameters ε and μ are also replaced with convolutional layers because CNN has been employed to model the HSI prior, which is as follows:

$$\hat{X}^{k+1} = T(X^k) + \varepsilon \cdot \text{IRN}(Y) + \varepsilon \mu \cdot \text{Spa_Spec}(X^k) \quad (11)$$

where $T(\cdot)$ presents the transformation layer of X^k . One convolutional layer is utilized in this article. $\text{IRN}(\cdot)$ indicates the initial restoration network block. All parameters, namely, ε and μ , are learned by CAMs. Details are presented later.

B. SRF-Guided Initial Restoration

As described in Section I, the SRFs can provide spectral relevance between MS and HS bands from an imaging point of view. Therefore, unlike the traditional deep learning-based methods, SRF guiding is introduced as an auxiliary operation, which can realize effective SSR performance. Auxiliary physical operations give a great deal of assistance to deal with image restoration in many types of research [40]–[43]. In the proposed CNN, a new SRF-guided IRN block is proposed to group bands by spectral radiation characteristics and reconstruct the initial SSR result X^0 with different operators. The SRF-guided initial restoration network is shown in Fig. 2.

The whole block is a two-layer CNN. Also, the reconstruction convolutional layers for different spectral ranges are identified separately using SRF as a guide. Details are as follows. First, the spectral gradients of RGB/MS images are computed to construct a data cube with a dimension of $W \times H \times (2c - 1)$, as shown in Fig. 3.

After that, the data cube is fed into a 3×3 convolutional layer to extract spectral features. These features are then fed into SRF-guided convolutional layers by grouping with spectral relevance according to SRFs. The spectral grouping is

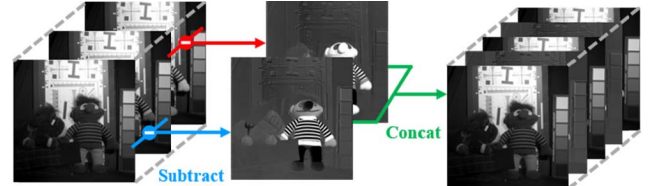


Fig. 3. Spectral gradient computation.

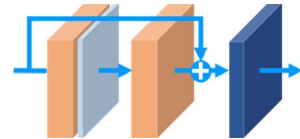


Fig. 4. SSN.

used to avoid reconstruction distortion caused by the excessive spectral difference between different channels. Nevertheless, it seems inevitable that there still will be some differences between bands in the same group. The proposed strategy ensures that intragroup bands reconstruction is determined by the same combination of multispectral channels. By roughly representing spectral relevance from the similarity of imaging according to SRFs, SRF-guided convolutional layers do not have to be adjusted for the same sensor, which improves the generalization of this module.

For example, in the CAVE data set, which consists of RGB images and HSIs with 31 bands, spectral ranges can be divided into three groups based on the band contribution in RGB imaging, including only contributing to the blue band, having contribution to blue and green bands, and contributing to green and red bands, which is proved to be the best by vast experiments. Then, the grouped spectral features are fed into convolutional layers. Therefore, SRF-guided convolutional layers play a role as spectral grouping restoration. In other words, HS channels with high spectral relevance will be constructed by the same convolution operator group.

With SRF as a guide, the IRN block can group the spectral bands with a high spectral correlation. This grouping avoids the introduction of irrelevant spectral information that disrupts spectral restoration.

C. Deep Spatial-Spectral Prior

As discussed in Section II-A, the HSI prior can be modeled by an SSN, which is shown in Fig. 4. The SSN comprises two

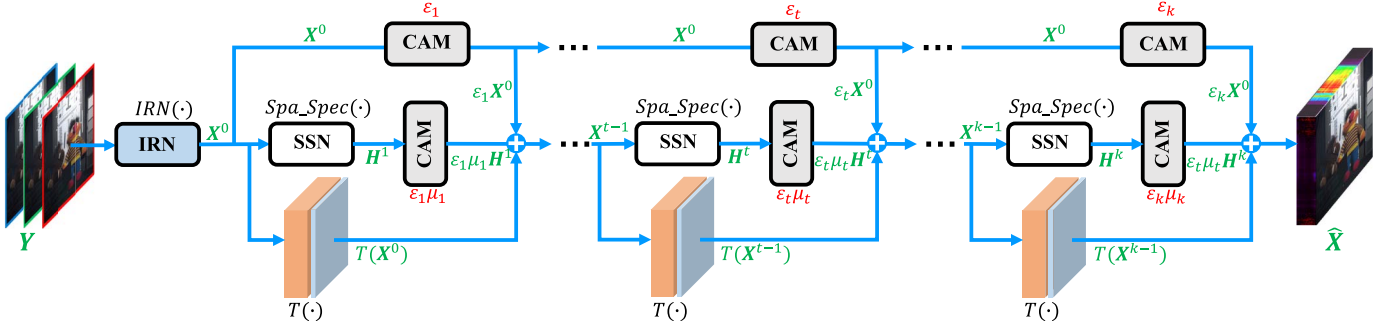


Fig. 5. Optimization stages of HSRnet.

subnetworks in series: one for spatial information extraction and the other for spectral feature extraction.

The intermediate reconstructed HSI is fed into the first 3×3 convolutional layer to compute for additional feature maps considering the influence of spatial neighborhood and transform the HSI data into a high-dimensional space. This transformation provides additional extracted features to the subsequent learning of spectral information. The second 3×3 convolutional layer is used as a selection for the next spectral optimization from the redundant features; besides, reducing the number of feature maps can accelerate the network calculation [44]. The last 1×1 convolutional layer achieves the fine-tuning of each spectral vector pixel-by-pixel. With the data-driven training, fine-tuning can be learned as spectral optimization processing. Furthermore, the 1×1 convolutional layer can significantly improve the effect of low-level image processing, which can further facilitate SSN learning of the HSI prior [45]. A skip connection adding the input to the output of the spatial network is also applied. This connection can accelerate network computation and simultaneously force the network to provide further attention to the changing details.

Equipped with SSNs, the proposed method can implicitly introduce an HS prior to further constrain the solution space and achieve improved SSR results.

D. Optimization Stages in HSRnet

With the application of the gradient descent algorithm and deep spatial-spectral prior, the SSR problem can be solved by updating X as (11), which is regarded as an optimization process. When the optimization is unfolded, a network comprising multiple stages can serve as an alternative to achieve optimization update in a deep learning manner, as shown in the optimization stages in Fig. 5.

The original RGB/MS image Y is first fed into the IRN block for an initial estimation $X^0 = \text{IRN}(Y)$. Given the initial HSI restoration X^0 , the iterative optimization, which can be trained to learn the HSI prior and match the spectral degradation model simultaneously, can be modeled in a feedforward manner. Three parts are needed for the k th updating as shown in (11). The first term is $T(X^{k-1})$, a spectral transformation preceding X^{k-1} , which is computed by a convolutional layer with a size of $C \times 3 \times 3 \times C$. The second term is $\varepsilon \cdot \text{IRN}(Y)$, which is the weighted initial estimation X^0 by ε . The last is $\varepsilon \mu \cdot \text{Spa_Spec}(X^{k-1})$, the $\varepsilon \mu$ -weighted result of H^k , which is the result from X^{k-1} , fed into the SSN for the HSI prior.

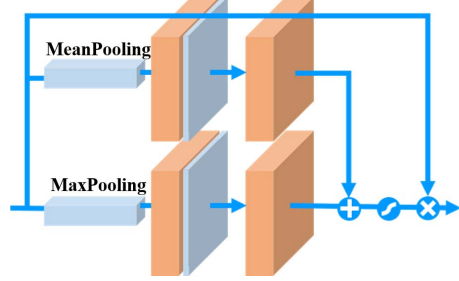


Fig. 6. CAM block.

The parameters ε and μ are learned by a block with attention mechanism. Details are provided later.

E. Attention-Based Parametric Self-Learning

The step size ε and the balance parameter μ change accordingly in each iteration to optimize the intermediate variable X^k iteratively. All the parameters in this article can be learned due to the backpropagation in training, which is a data-driven manner without manual intervention. However, parameters in traditional methods are all similar for different spectral channels. This similarity may be an inappropriate way for spectral bands with different radiance characteristics because of different optimal signal-to-noise ratios and different spectral information introduced in the input data. Considering the radiance differences in different bands and the good performance in the channel weighting of CAM, the CAM blocks are applied to the proposed HSRnet, as shown in Fig. 6. CAM can help HSRnet focus on bands that need urgent optimization with high weights by exploiting the interchannel relationship of features.

The CAM block comprises two pooling layers with max pooling and mean pooling, two 3×3 convolutional layers, and a sigmoid function. First, the reconstructed HSI is fed into the pooling layer to extract global weights. After pooling layers, the global weights are forwarded to two convolutional layers and summed. Finally, the channel weights are activated by a sigmoid function before elementwise multiplication.

Introducing channel attention, HSRnet can easily learn different parameters as a vector of each iteration rather than a fixed value. This condition can ensure the adaptive weight adjustment of the network in spectral optimization and the realization of an improved reconstruction effect.

TABLE I

RUNNING TIME OF DIFFERENT LOSSES		
	With CPU	With GPU
SAM Loss	2.6642 s	-
Proposed Loss	1.4611s	0.03748 s

F. Fast Joint Spatial–Spectral Loss

The L1 loss and SAM loss functions are applied in this article as shown in the following to enhance spectral resolution and preserve the spatial detail simultaneously

$$L = |\hat{X} - X| + \alpha \sum_{j=1}^{WH} \cos^{-1} \left(\frac{\hat{X}^j X^j}{\sqrt{\hat{X}^{jT} \hat{X}^j} \sqrt{X^{jT} X^j}} \right) \quad (12)$$

where \hat{X} is the reconstructed HSI, X is the ground truth, \hat{X}^j presents the recovered spectral vector in j th pixel, X^j is the ground truth, and α is a balance parameter. However, the application of SAM loss is difficult in practice due to computational complexity and the inability of GPU-accelerated computation as a vector form. Inspired by [46], a transformed RMSE loss is utilized, which is shown as

$$L = |\hat{X} - X| + \alpha \cos^{-1} \left(1 - \frac{1}{2} \|\hat{X}' - X'\|^2 \right) \quad (13)$$

where \hat{X}' is the reconstructed HSI unitized pixel-by-pixel and X' is the unitized ground truth.

Thus, SAM loss can be calculated as a tensor form. This calculation allows parallel computation with GPU, which will be swift in learning as shown in Table I.

III. EXPERIMENTAL RESULTS

A. Experimental Setting

1) *Comparison Methods*: The proposed method is compared with the related algorithms of SSR without HSI required as input, including Arad [18], A+ [19], DenseUnet [28], CanNet [29], HSCNN+ [30], and sRCNN [31]. The compared methods involve the dictionary and deep learning-based methods, which are currently state of the art in SSR. The models of A+ and Arad are reproduced through a program coded by Wu *et al.* [19].

2) *Quantitative Metrics*: Four quantitative image quality metrics, including correlation coefficient (CC), peak signal-to-noise ratio (PSNR), structural similarity (SSIM) [48], and SAM [49], are utilized to evaluate the performance of all comparison methods quantitatively. CC, PSNR, and SSIM are indexes that show the spatial fidelity of the reconstructed HSIs, which are computed on each channel and averaged over all spectral bands. Results with their large values indicate that the method is effective for maintaining spatial detail. Meanwhile, SAM evaluates the spectral preservation of the algorithms, showing improved spectral fidelity when the SAM is small.

3) *Implementation Detail*: The optimization stage number k is set to 9, which shows the best SSR effect among the following tests. The learning rate is set to 0.001, and the gradient-based optimization algorithm based on adaptive estimates of low-order moments (Adam [50]) is employed to train HSRnet.

TABLE II

NUMERICAL COMPARISON OF FOUR QUANTITATIVE IMAGE QUALITY METRICS BETWEEN RESULTS ON THE CAVE DATA SET

Methods	CC	PSNR	SSIM	SAM
Arad	0.9486	24.4613	0.7913	21.3129
A+	0.9873	32.8830	0.9297	20.5403
DenseUnet	0.9907	32.5510	0.9642	8.1915
CanNet	0.9925	33.5975	0.9685	8.6435
HSCNN+	0.9934	34.4354	0.9766	7.8048
sRCNN	0.9916	34.3669	0.9731	9.0175
HSRnet	0.9935	34.4903	0.9771	7.6208

The tradeoff parameter α for the loss function is set to 0.0001. The models are trained by the Pytorch framework running in the Windows 10 environment with 16-GB RAM and one Nvidia RTX 2080 GPU.

4) *Experimental Data Set*: The proposed HSRnet is evaluated by using the HSIs from CAVE [47] and remote sensing data sets.

a) *CAVE Data Set*: CAVE data set, which comprises 32 scenes with a size of 512×512 , is a popular HSI data set in HSI processing. All the HSIs in the CAVE data set cover the spectral range from 400 to 700 nm with a 10-m spectral resolution containing 31 bands. Moreover, the RGB images covering the same scene as HSI data are available.

A total of 26 HSIs and the corresponding RGB images are randomly selected to prepare the training samples, and each image is split into 16 patches with a size of 128×128 . Data augmentation is employed in this experiment because the insufficient training data are unfavorable to model training. The original training samples are flipped and rotated to increase the training data by eight times. The six remaining images are utilized for the test. The test images are shown in Fig. S1, which is in the Supplementary Material.

b) *Remote Sensing Data Set*: i) *Sen2OHS Data Set*: Images from four Chinese Orbita hyperspectral satellites (OHS) with 10-m spatial resolution are selected as HSIs to build a remote sensing data set. OHS captures the HSIs in the spectral range from 400 to 1000 nm with 2.5-nm increments, but the HSI data sent to users are sampled to 32 bands.

The rich spectral information in OHS data with the 10-m spatial resolution is of considerable importance for application. However, free OHS data are mostly unavailable because of commerciality. This unavailability limits the HS data sources for researchers. Meanwhile, some MS images, such as Sentinel-2 bands with the same spatial resolution as OHS data (bands 2–4 and 8), are available for free. Thus, the Sen2OHS data set is simulated to evaluate the SSR effect of the proposed model on the remote sensing data.

Sentinel-2 MSIs are simulated from OHS HSIs by using Hysure [38] with the SRF of Sentinel-2 and OHS-A to reduce the errors caused by geographic registration and the inconsistency of acquiring time between Sentinel-2 and OHS data. Furthermore, 6000 OHS HSIs with a size of 128×128 are selected for training from the Competition in Hyperspectral Remote Sensing Image Intelligent Processing Application.¹ The location of these images is shown in

¹The data set can be download at <https://ohs.obtdata.com/#/dataDownload>

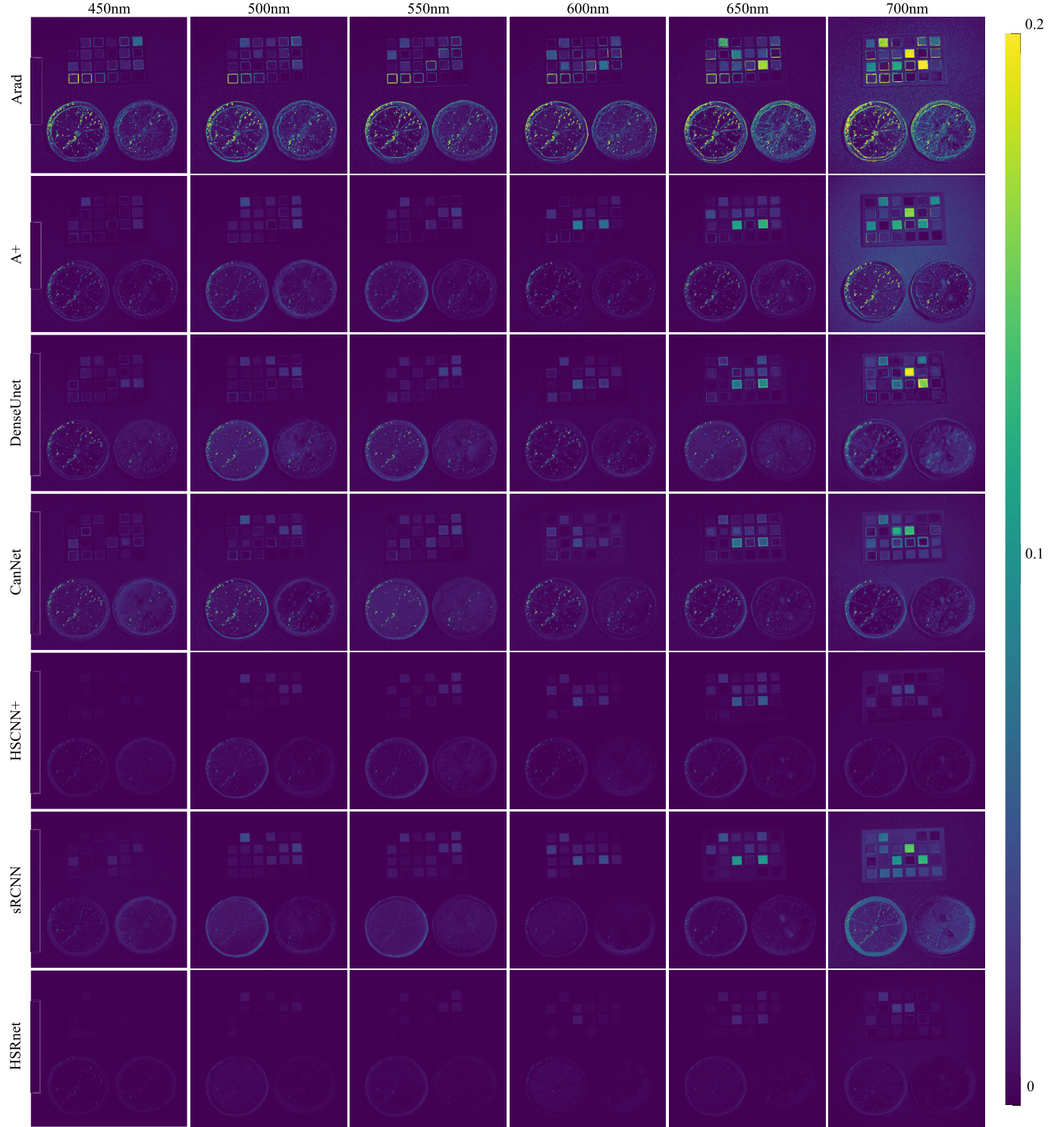


Fig. 7. Absolute differences of “Lemon Slices” image from the CAVE data set. Along 450, 500, 550, 600, 650, and 700 nm, the absolute differences between the reconstructed images and the ground truth are given. Each row from top to bottom is the result of Arad, A+, DenseUnet, CanNet, HSCNN+, SRCNN, and the proposed HSRnet.

Fig. S2 in Supplementary Material. And the testing images are randomly selected in Xiongan New Area, Hebei Province, China, as shown in Fig. S3.

ii) HR Simulation Data Set Based on Sen2OHS: Besides, to better verify the performance of models restoring spectral channels at different scales, three more data sets with an HR are also simulated based on Sen2OHS, including Xiongan,

Washington dc Mall, and Chikusei. Partial data of them are shown in Fig. S4 in Supplementary Material. The Xiongan data set was an aerial image covered rural in Matiwan Village, Xiongan New Area, China, with a size of 3750×1580 . The spectral range of the Xiongan data set is 400–1000 nm, with 250 bands and a spatial resolution of 0.5 m. The Washington DC Mall data set [51] was acquired by the HYDICE airborne

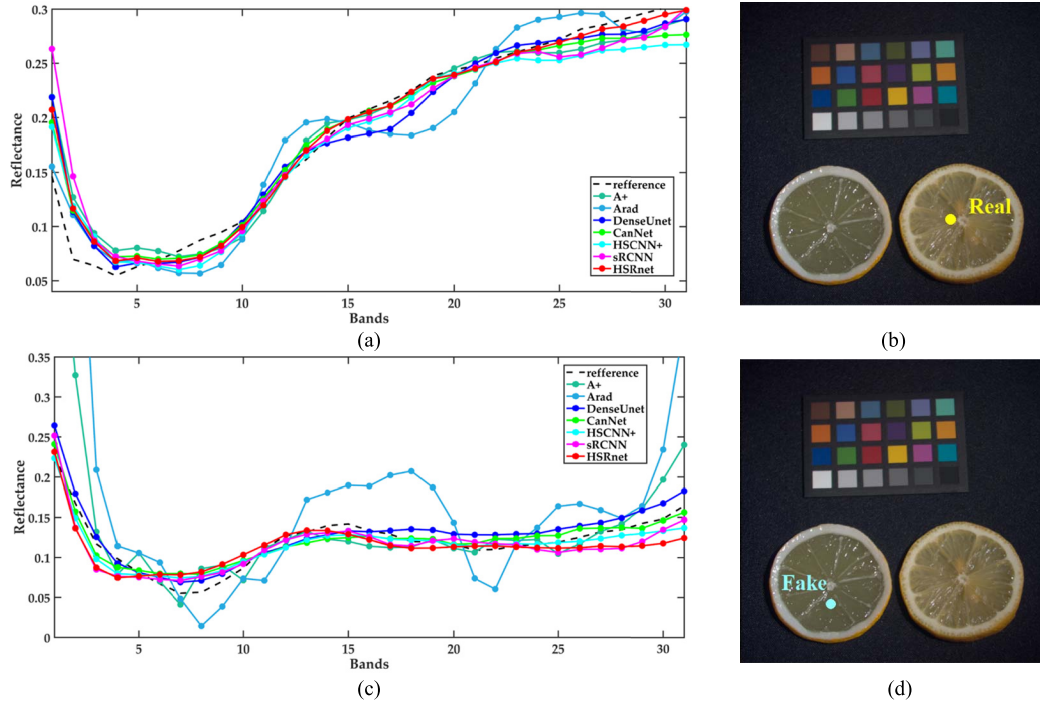


Fig. 8. Reflectance of “Lemon Slices” images from the CAVE data set at the fake and real lemon locations. (a) Reflectance at the real lemon slice location. (b) Real lemon slice location. (c) Reflectance at the fake lemon slice location. (d) Fake lemon slice location.

sensor and with a size of $1280 \times 307 \times 210$, covering the spectral wavelength from 400 to 2500 nm, and the spatial resolution is lower than Xiongan and close to Chikusei. The Chikusei data set was taken by the Headwall Hyperspec-VNIR-C imaging sensor over agricultural and urban areas in Chikusei, Japan, with a size of 2517×2335 [52]. It contains 128 spectral bands ranging from 363 to 1018 nm with a spatial resolution of 2.5 m. In the experiments, the spectral channels are downsampled to the same of OHS and Sentinel-2 by Hysure.

B. Results on CAVE Data Set

1) *Quantitative and Visual Results:* The quantitative results over six testing images are shown in Table II, where the best results are in red bold and the second best is in blue. From the four quantitative image quality indexes, the deep learning-based methods show more remarkable amelioration in the spectral preservation than that in dictionary learning-based methods. Moreover, A+ performs well in spatial fidelity and is more highly improved compared with Arad. Also, the proposed HSRnet shows superior performance in spatial and spectral evaluation simultaneously.

In comparison to dictionary learning-based methods, the HSRnet achieves an average of 63.57% reduction in SAM and an average of 22.94% increase in PSNR. These findings illustrate that HSRnet can achieve effective spectral enhancement and maintain spatial information. Compared with other deep learning-based methods, HSRnet still shows some advantages in all indexes. HSCNN+ and sRCNN also show good spatial fidelity but get a worse spectral evaluation.

Difference maps (DMs) between the reconstruction results and the ground truth are constructed to evaluate the results

TABLE III
NUMERICAL COMPARISON OF FOUR QUANTITATIVE IMAGE QUALITY METRICS BETWEEN THE METHODS IN THE SEN2OHS DATA SET

Methods	CC	PSNR	SSIM	SAM
Arad	0.8149	22.4581	0.5631	11.0670
A+	0.8592	24.4238	0.6924	9.5847
DenseUnet	0.9498	26.7262	0.8769	8.3135
CanNet	0.9621	28.1981	0.8901	7.4233
HSCNN+	0.9593	28.8117	0.9164	6.9076
sRCNN	0.9689	29.2940	0.9389	6.5788
HSRnet	0.9725	28.9801	0.9344	6.8410

intuitively, as shown in Fig. 7. Six channels with wavelengths of 450, 500, 550, 600, 650, and 700 nm are selected. Fig. 7 shows that Arad’s result shows poor performance in spatial detail, as indicated in the background and the lemon pulp among all the presented bands. A+ obtains a better effect compared with that of Arad and even better than DenseUnet at some bands, such as 450 and 550 nm. CanNet shows a high difference in the edges. HSCNN+ can get good performance in several bands. However, HSRnet obtains DMs with the lowest value, which indicates that HSRnet achieves the best performance in SSR. As seen in DMs, HSRnet can adaptively accomplish spectral enhancement of different targets on the palette or the lemon slice. All methods perform poorly at the wavelength of 700 nm because of the insufficient spectral information.

2) *Discussion on Fake and Real Lemon Slices:* Because there are fake and real lemon slices in the testing images, the reconstruction effects of methods at fake and real lemon slices are also presented. As shown in Fig. 8, the reflectance of real and fake lemon slices completely varies among bands 15–31, namely the wavelength from 540 to 700 nm. The spectral curve

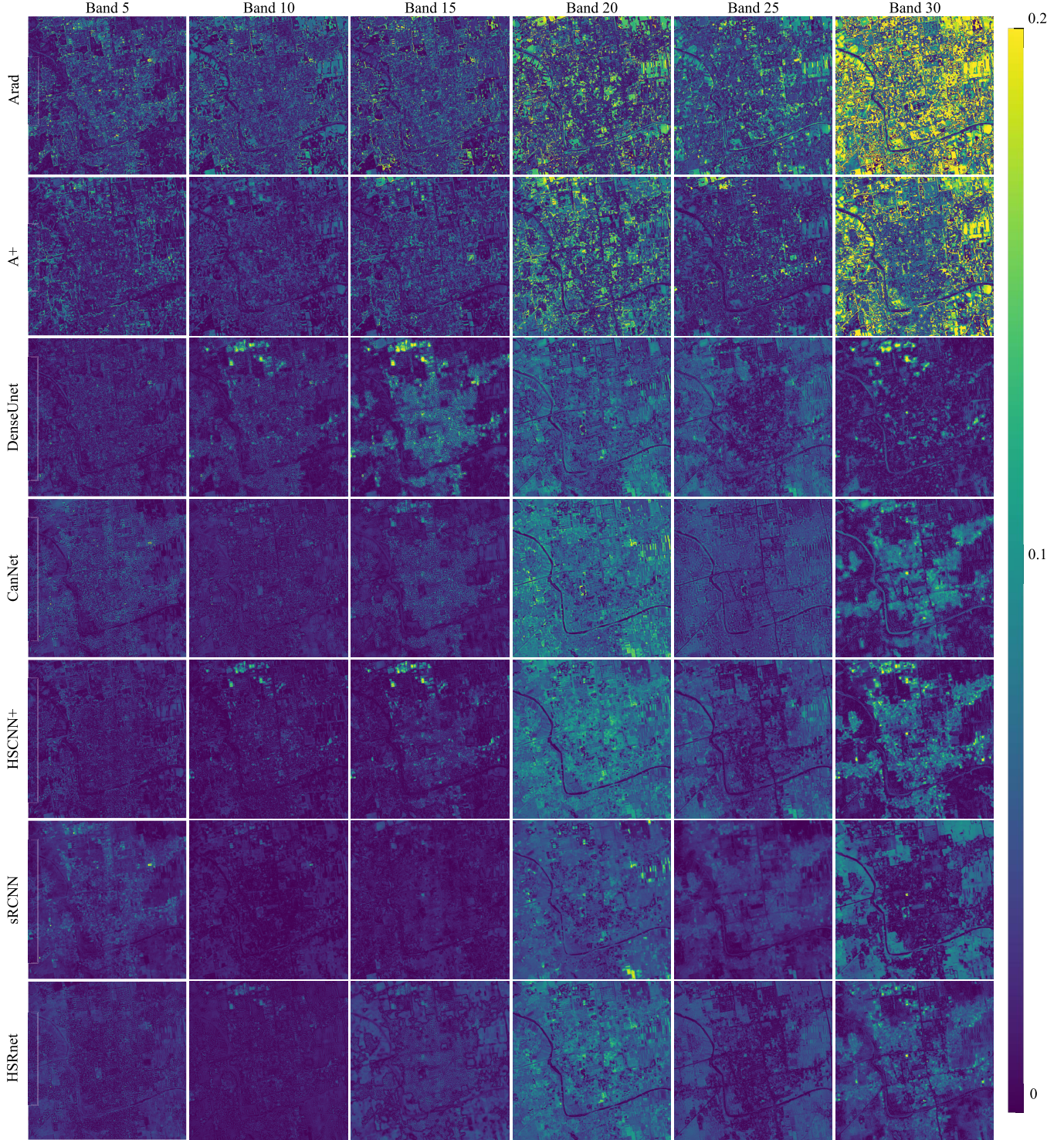


Fig. 9. Absolute differences of “Urban” image from the Sen2OHS data set. Along with bands 5, 10, 15, 20, 25, and 30, the absolute differences between the reconstructed images and the ground truth are given. Each row from top to bottom is the result of Arad, A+, DenseUnet, CanNet, HSCNN+, sRCNN, and the proposed HSRnet.

of real lemon still increases after band 15. However, the spectral curve of fake lemon initially drops and then rises. In this case, deep learning-based methods can adaptively reconstruct the spectral detail of fake and real lemon slices separately. This reconstruction benefits from the powerful learning capability of CNNs, but Arad and A+ show poor performance in these bands. Although other deep learning-based algorithms can

achieve good performance on distinguishing the spectrum of fake and real objects, the results of HSRnet show the highest similarity to the ground truth.

C. Results on Remote Sensing Data Set

The proposed model is also verified on the remotely sensed data set. Furthermore, four quantitative image quality indexes

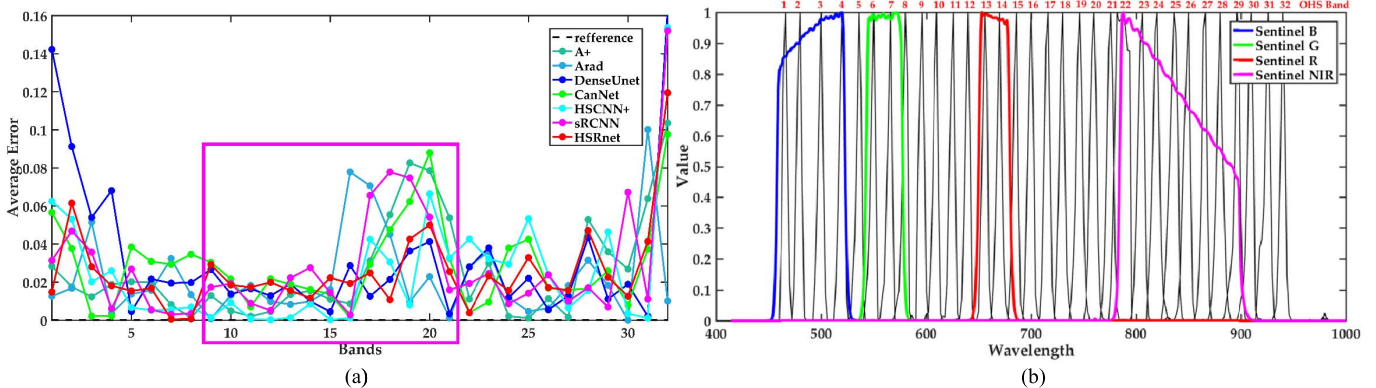


Fig. 10. (a) Average error of the results on the “Urban” image. Framed by magenta, results on bands 9–21 of all methods show a poor tendency because of limited related spectral information in the input Sentinel-2 data. (b) Different SRFs of Sentinel-2 and OHS-A, which are used to help explain the phenomenon presented in (a).

are employed to evaluate experimental results in the simulated experiments, including Sen2OHS data set and three HR simulation data sets. After the simulated experiments, the trained model will be utilized to enhance the spectral resolution of real Sentinel-2 data. Moreover, a classification is presented to demonstrate the reliability of the reconstructed HSIs.

1) Quantitative and Visual Results:

a) *Sen2OHS Data Set*: Table III shows the quantitative assessment results of testing images in the Sen2OHS data set. In contrast to the natural images, targets in remote sensing images are various and complex, resulting in poor spatial fidelity for all methods. The spectral preservation is improved because of the less color variation between targets than natural images. A+ and Arad show a sharp decline in CC, PSNR, and SSIM, which indicates a poor generalization effect. It is noted that the training samples of Arad and A+ are the same as those of deep learning-based methods, which are not divided into different domains unlike that of the CAVE data set because an effective model should be able to reconstruct images in different scenes adaptively with unified training samples.

The proposed HSRnet improves the average CC, PSNR, and SSIM value by 16.18%, 23.63%, and 48.85%, respectively, compared with Arad and A+. The improvement of SAM is beyond 33.75%. Compared with four deep learning methods, HSRnet shows a certain advantage in both spatial fidelity and spectral preservation. Surprisingly, sRCNN gains a tiny advantage over HSRnet, which is benefited by the spectra-by-spectra band optimization with huge computation.

The DMs of the selected testing image named “Urban” are shown in Fig. 9. Six bands, including bands 5, 10, 15, 20, 25, and 30, are displayed. The “Urban” image comprises rivers, farmlands, buildings, and other features, providing a considerable challenge to SSR. From the DMs of band 30, the spectral enhancement of farmlands with regular geometric shapes but diverse color brightness is difficult for dictionary learning-based methods. However, the sporadic buildings obtain improved spectral fidelity in A+ and Arad. For deep learning-based methods, with strong learning capability of different features, recovering the target with regular geometric shapes is easy, such as farmlands, streets, and rivers, but the recovery of various buildings, as shown in the results of deep learning-based methods on bands 20 and 30, shows

TABLE IV

NUMERICAL COMPARISON OF FOUR QUANTITATIVE IMAGE QUALITY METRICS BETWEEN THE RESULTS ON THREE HR SIMULATION DATA SETS

Dataset	Method	CC	PSNR	SSIM	SAM
Xiongan	DenseUnet	0.9847	42.4634	0.9814	0.9217
	CanNet	0.9946	48.3492	0.9950	0.8029
	HSCNN+	0.9942	48.4972	0.9959	0.7888
	sRCNN	0.9954	49.8814	0.9973	0.7623
	HSRnet	0.9963	50.7362	0.9973	0.7196
Washington DC Mall	DenseUnet	0.9927	39.7343	0.9848	1.8808
	CanNet	0.9987	47.8736	0.9971	1.1805
	HSCNN+	0.9986	47.5770	0.9972	1.0983
	sRCNN	0.9989	48.5363	0.9978	1.0179
	HSRnet	0.9992	50.4457	0.9983	0.9395
Chikusei	DenseUnet	0.9897	39.2096	0.9809	4.0650
	CanNet	0.9967	44.2579	0.9933	3.6732
	HSCNN+	0.9947	42.5542	0.9908	3.4254
	sRCNN	0.9955	43.4017	0.9924	3.5490
	HSRnet	0.9968	44.7133	0.9941	3.4528

unsatisfactory effect. This may be due to the inconsistently different geometric shapes of the same ground feature, which confuses CNN and mistakes them as different features. However, the results of the proposed HSRnet show lower error and less detail loss. Although sRCNN gets the best quantitative indexes, HSRnet shows more balanced visual results in different bands.

Fig. 10(a) shows the average error of compared methods. The curve trend indicates that the SSR effect of the bands at the edge of the spectral coverage is worse than that of other bands. This finding has also been verified on the CAVE data set, which is due to the limited spectral information of bands at the edge of the spectral range obtained from the input MSIs. Furthermore, all the compared methods yield slightly worse results on bands 9–21, as framed by magenta. As shown in Fig. 10(b), the spectral range of Sentinel-2 and OHS-A is incompletely covered. Bands 9–12, 16–20, and 30–32 of the OHS data are not covered by Sentinel-2 SRF, thus yielding bands with poor spectral fidelity. However, with the SRF as a guide, HSRnet has good spectral reconstruction capability when spectral information of the relevant bands is deficient, which is shown in the figure with lower average errors in the form of fluctuations instead of a surge.

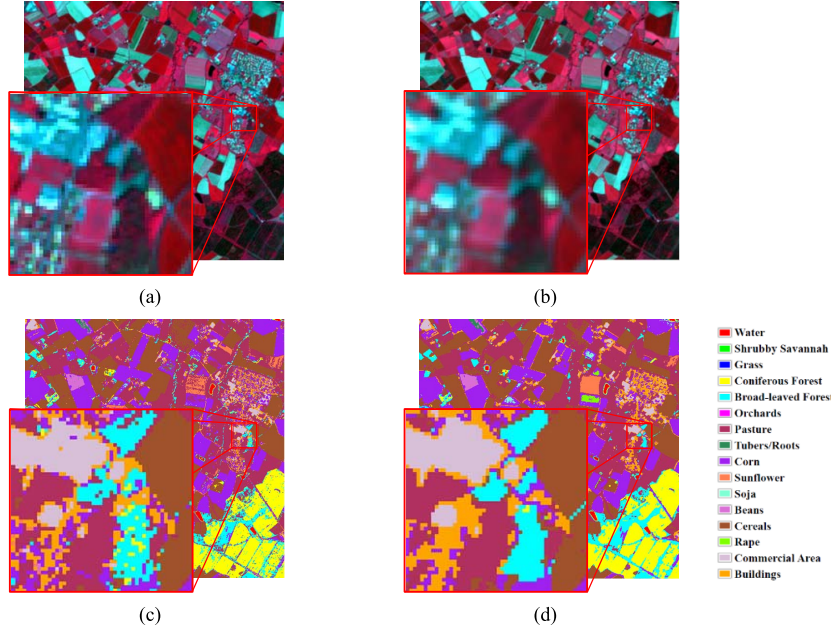


Fig. 11. Classification comparison on the real Sentinel-2 data and the reconstructed HSI by HSRnet. (a) Original Sentinel-2 data. (b) HSI reconstructed by HSRnet. (c) Original classification. (d) Classification of the reconstructed HSI.

b) HR Simulation Data Sets: To further compare the effect of the deep learning-based methods in different scales, synthetic data sets with finer spatial details, including Xiongan, Washington DC Mall, and Chikusei, are utilized. Quantitative results are shown in Table IV.

On these HR data sets, SSR becomes easier to achieve. With purer spectral information in HR training samples, deep learning-based methods can recover spectra more accurately, as shown in Table IV. Also, sRCNN shows good applicability in remote sensing data sets because of spectra-by-spectra optimization steps. Compared with sRCNN, the proposed HSRnet can get better performance with lower computational complexity. With the results of data sets at four different scales in remote sensing, the proposed HSRnet shows great stability and superiority over other deep learning-based algorithms in spectral fidelity.

2) Classification Results on Real Data: Due to the good performance demonstrated on the remote sensing data set, the trained HSRnet model is used on real Sentinel-2 data with a 10-m spatial resolution to verify the reliability of the increased spectral information compared with the original MSI. We choose the classification experiments to evaluate it. The image is selected in the south of Nantes, France, with a size of 512×512 . The comparison results are shown in Fig. 11. The HSI is displayed with bands 27, 13, and 8 and the real Sentinel-2 data is shown with bands 8, 4, and 3, where the vegetation is red.

The features are classified into 16 classes by using the support vector machine (SVM), as shown in the legend in Fig. 11. Additional spectral information is introduced to help combine the adjacent similar objects, and the classification results of the reconstructed HSI show less discrete objects.

The quantitative evaluation also shows that the increased spectral information recovered by HSRnet can help classi-

TABLE V
OVERALL ACCURACY AND KAPPA COEFFICIENT OF CLASSIFICATIONS

	OA	Kappa
Original MSI	70.74%	0.6296
Reconstructed HSI	73.22%	0.6619

fication, as presented in Table V. The classification results demonstrate the improvements in OA and Kappa due to the additional spectral information in the reconstructed HSI. This improvement indicates that the proposed SSR method can accurately recover spectral information on the real data set.

D. Discussion

This section discusses the reliability of the proposed HSRnet, including ablation study and computational speed analysis.

1) Ablation Study: The efficiency of the strategies of the proposed HSRnet, including optimization stages, parametric self-learning based on CAM, SRF-guided initial restoration network, and fast joint spatial–spectral loss, is first discussed, as shown in Table VI. A 19-layer Resnet [24] is chosen as a baseline. OS, CAM, SRF, and SAM Loss represent the aforementioned strategies, and the details will be provided later.

a) Optimization Stages: Compared with Resnet, HSRnet with only optimization stages (namely, HSRnet w/o CAM in Table VI) shows substantially high superiority in spatial and spectral fidelity. Compared with DenseUnet, the proposed network with physical interpretability shows a slight advantage without the help of other strategies.

b) CAM: Comparing HSRnet without SRF with HSRnet without CAM, HSRnet with parametric self-learning based on CAM shows improved spatial fidelity and spectral enhancement due to the capability to learn parameters adaptively for different iterations and bands.

TABLE VI
ABLATION STUDY OF THE PROPOSED STRATEGIES ON THE CAVE DATA SET

	OS	CAM	SRF	SAMLoss	CC	PSNR	SSIM	SAM
ResNet	✗	✗	✗	✗	0.9843	28.4483	0.9415	11.4720
DenseUnet	-	-	-	-	0.9907	32.5510	0.9642	8.1915
HSRnet w/o CAM	✓	✗	✗	✗	0.9919	33.3288	0.9674	8.2279
HSRnet w/o SRF	✓	✓	✗	✗	0.9930	34.2748	0.9741	8.0927
HSRnet w/o SAMLoss	✓	✓	✓	✗	0.9933	34.3467	0.9742	7.8506
HSRnet	✓	✓	✓	✓	0.9935	34.4903	0.9771	7.6208

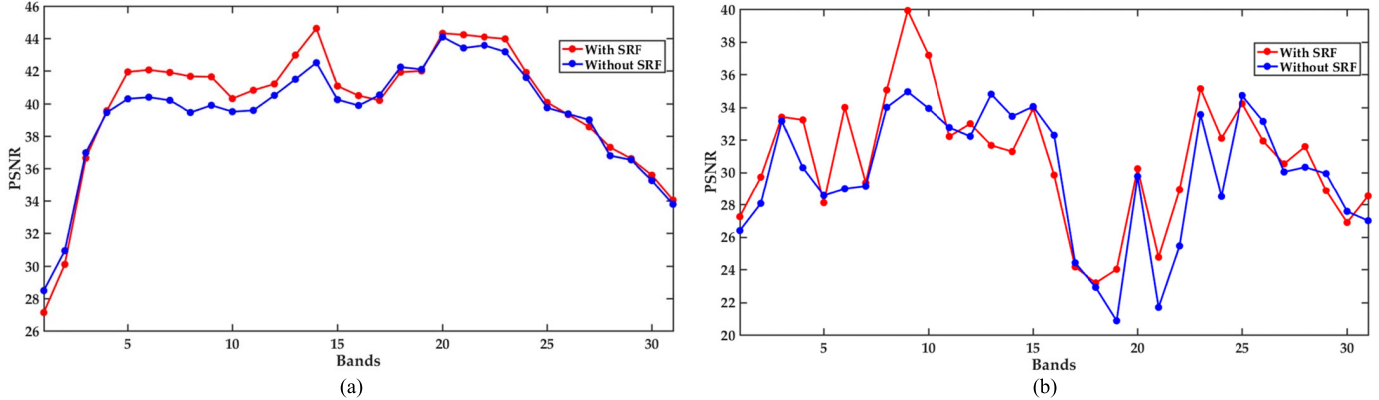


Fig. 12. PSNR of results reconstructed with SRF as a guide and without SRF on two data sets. (a) Comparison on CAVE data set. (b) Comparison on Sen2OHS data set.

c) *SRF-Guided IRN*: With the SRF as a guide, HSRnet shows tiny spatial improvements but substantially good spectral maintaining as shown in the values of SAM (i.e., HSRnet w/o SAMLoss in Table VI). Furthermore, the comparison with HSRnet without SRF on the CAVE data set is shown in Fig. 12. As shown in Fig. 12(a), the PSNR of results reconstructed by the model with SRF as a guide is higher than the model without an SRF guide. This finding shows that the SRF guide can help HSRnet achieve improved performance. Fig. 12(b) shows the same conclusion on the remote sensing data set.

d) *Spatial–Spectral Loss Function*: With SAMLoss, the proposed HSRnet shows some improvement not only on SAM but also on other metrics of spatial fidelity. It states that considering the spectral loss with spatial loss function, the spatial fidelity and spectral preservation can be mutually reinforced.

2) *Computational Speed Analysis*: Deep learning-based methods can achieve satisfying spectral enhancement on the CAVE and Sen2OHS data sets due to their strong nonlinear mapping capability, and the parameter number is very important to them. For example, as the parameter number increases, CNN can reach effective performance without changing the structure by computing additional features in convolutional layers. Thus, the comparison between deep learning-based methods in parameter number and running time is performed with similar feature numbers.

Table VII lists the parameter numbers, floating-point operations (FLOPs), and training and test time of deep learning methods. Training and test time are all counted on the CAVE data set. DenseUnet uses numerous parameters in down-and-up stages due to dense blocks, while most effort is put into optimization stages in HSRnet. Besides, CanNet

TABLE VII
COMPUTATIONAL SPEED ANALYSIS OF DEEP LEARNING-BASED METHODS ON THE CAVE DATA SET

	DenseUnet	sRCNN	CanNet	HSCNN+	HSRnet
Params	1360.1K	789.3K	163.0K	915.1K	769.7K
FLOPs	3.02×10^{10}	5.96×10^{12}	3.97×10^{10}	2.23×10^{11}	1.79×10^{11}
Training	68655s	146539s	49285s	57805s	30831s
Test	1.2598s	4.5950s	1.2387s	1.7996s	1.5364s

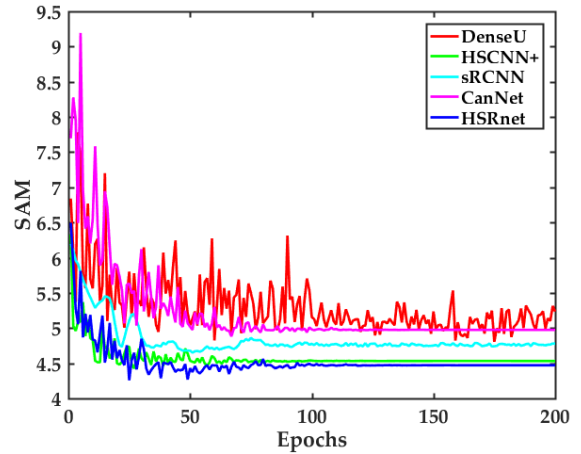


Fig. 13. Validation loss of deep learning-based methods.

requires the least parameters because it works as a shallow network. Although the parameter number in DenseUnet is approximately twice as many as the proposed HSRnet in total, HSRnet shows better performance in SSR compared with DenseUnet. FLOPs show the algorithm complexity by FLOPs. With pixel-by-pixel optimization, sRCNN gets the highest FLOPs although the parameter number is similar to HSRnet, which leads to a long running time. DenseUnet benefits from

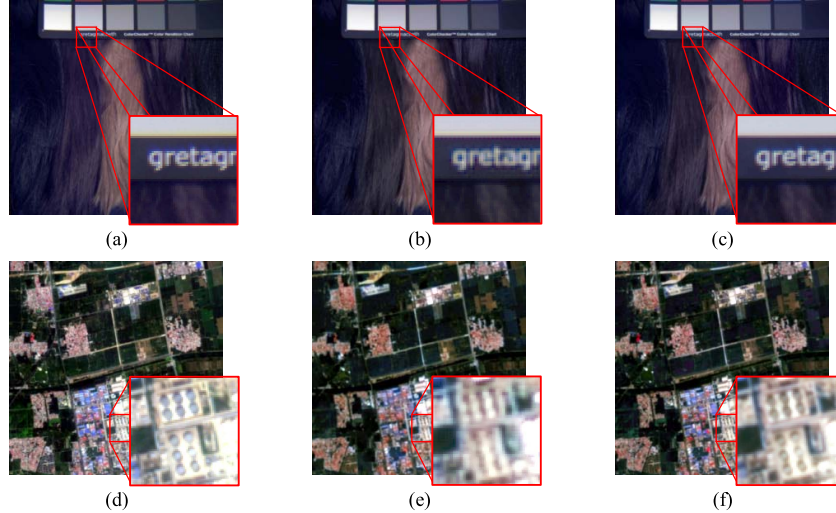


Fig. 14. Partially enlarged details of the results on “Hair” and “Industrial District” image. (a) Reference “Hair” image in the CAVE data set is shown by bands 14, 7, and 2. (b) Result of DenseUnet is shown by the same band combination. (c) Result of HSRnet. (d) Ground truth of the “Industrial District” image in the Sen2OHS data set is shown in bands 14, 7, and 2. (e) Result of DenseUnet shown by the same band combination. (f) Result of HSRnet.

the downsampling and upsampling to get the fewest FLOPs. Although DenseUnet can train an epoch faster than HSRnet, it converges at 200 epochs. Without downsampling to fast calculation, HSRnet spends more training time in each epoch but converges earlier than that of other networks, as shown in Fig. 13.

As discussed above, DenseUnet can accelerate the calculation by downsampling the input images. However, this acceleration compromises spatial details, as shown in Fig. 14. Whether on the CAVE or Sen2OHS data set, DenseUnet shows spatial blurry effects, whereas HSRnet can maintain good spatial fidelity with rich details, such as the cylindrical buildings in Sen2OHS results and the clear letter edges in CAVE results. Furthermore, the HSRnet results suffer from mild spatial degradation on the Sen2OHS data set. Notably, the spatial resolution of the captured OHS-A data is not accurately 10 m. This value is slightly coarser than that of Sentinel-2, resulting in spatial degradation.

The proposed HSRnet has acceptable parameter numbers and computation complexity but gets the best SSR performance. Furthermore, considering the effect and running time, HSRnet maintains more spatial details using fewer parameters and acceptable test time. Furthermore, HSRnet realizes early convergence, although the training time of HSRnet is longer than that of other methods in one iteration, resulting in less total training time. Thus, a conclusion can be drawn that building CNN with physical logic is superior to using data-driven CNN.

IV. CONCLUSION

This article presents an SRF-guided optimization-driven SSR network with spatial-spectral prior to enhance the spectral information of the MS/RGB image. The traditional gradient descent-based algorithm is transformed into an end-to-end CNN with the help of deep spatial-spectral prior. The proposed HSRnet² groups the spectral similar bands

using the physical information and the SRF to reconstruct different spectral ranges instead of the traditional black-box data-driven CNN. Using the CAM blocks to learn parameters rather than a manual setting can automatically adjust the weights for different channels rather than a fixed value to the entire image. Moreover, the proposed HSRnet transforms the optimization model into a data-driven model. This model provides CNN with physical interpretability and facilitates flexible learning of optimization parameters in an end-to-end manner. Experimental results on natural and remotely sensed data sets confirm the feasibility and superiority of the proposed method. Furthermore, as shown in both data sets, especially in Sen2OHS data set, the spectral coverage between input and output data plays an important role in the model effect. Thus, the effective utilization of MS bands with different spatial resolutions to reach complete coverage of spectral information and achieve spatial-spectral SR is a direction of our future works.

REFERENCES

- [1] J. Li, J. M. Bioucas-Dias, and A. Plaza, “Spectral-spatial hyperspectral image segmentation using subspace multinomial logistic regression and Markov random fields,” *IEEE Trans. Geosci. Remote Sens.*, vol. 50, no. 3, pp. 809–823, Mar. 2012.
- [2] M. Fauvel, Y. Tarabalka, J. A. Benediktsson, J. Chanussot, and J. C. Tilton, “Advances in spectral-spatial classification of hyperspectral images,” *Proc. IEEE*, vol. 101, no. 3, pp. 652–675, Mar. 2013.
- [3] D. Manolakis and G. Shaw, “Detection algorithms for hyperspectral imaging applications,” *IEEE Signal Process. Mag.*, vol. 19, no. 1, pp. 29–43, Jan. 2002.
- [4] A. A. Nielsen, “The regularized iteratively reweighted MAD method for change detection in multi- and hyperspectral data,” *IEEE Trans. Image Process.*, vol. 16, no. 2, pp. 463–478, Feb. 2007.
- [5] H. V. Nguyen, A. Banerjee, and R. Chellappa, “Tracking via object reflectance using a hyperspectral video camera,” in *Proc. IEEE Comput. Soc. Conf. Comput. Vis. Pattern Recognit. Workshops (CVPRW)*, San Francisco, CA, USA, Jun. 2010, pp. 44–51.
- [6] A. F. H. Goetz, G. Vane, J. E. Solomon, and B. N. Rock, “Imaging spectrometry for earth remote sensing,” *Science*, vol. 228, no. 4704, pp. 1147–1153, 1985.
- [7] J. M. Bioucas-Dias, A. Plaza, G. Camps-Valls, P. Scheunders, N. Nasrabadi, and J. Chanussot, “Hyperspectral remote sensing data analysis and future challenges,” *IEEE Geosci. Remote Sens. Mag.*, vol. 1, no. 2, pp. 6–36, Jun. 2013.

²The code can be found at <https://github.com/JiangHe96/HSRnet>

- [8] Q. Yuan, Q. Zhang, J. Li, H. Shen, and L. Zhang, "Hyperspectral image denoising employing a spatial-spectral deep residual convolutional neural network," *IEEE Trans. Geosci. Remote Sens.*, vol. 57, no. 2, pp. 1205–1218, Feb. 2019.
- [9] S. Tzoumas, N. Deliolanis, S. Morscher, and V. Ntziachristos, "Unmixing molecular agents from absorbing tissue in multispectral optoacoustic tomography," *IEEE Trans. Med. Imag.*, vol. 33, no. 1, pp. 48–60, Jan. 2014.
- [10] T. Akgun, Y. Altunbasak, and R. M. Mersereau, "Superresolution reconstruction of hyperspectral images," *IEEE Trans. Image Process.*, vol. 14, no. 11, pp. 1860–1875, Nov. 2005.
- [11] Y. Gu, Y. Zhang, and J. Zhang, "Integration of spatial-spectral information for resolution enhancement in hyperspectral images," *IEEE Trans. Geosci. Remote Sens.*, vol. 46, no. 5, pp. 1347–1358, May 2008.
- [12] R. C. Hardie, M. T. Eismann, and G. L. Wilson, "MAP estimation for hyperspectral image resolution enhancement using an auxiliary sensor," *IEEE Trans. Image Process.*, vol. 13, no. 9, pp. 1174–1184, Sep. 2004.
- [13] R. Kawakami, Y. Matsushita, J. Wright, M. Ben-Ezra, Y.-W. Tai, and K. Ikeuchi, "High-resolution hyperspectral imaging via matrix factorization," in *Proc. CVPR*, Providence, RI, USA, Jun. 2011, pp. 2329–2336.
- [14] N. Akhtar, F. Shafait, and A. Mian, "Bayesian sparse representation for hyperspectral image super resolution," in *Proc. IEEE Conf. Comput. Vis. Pattern Recognit. (CVPR)*, Boston, MA, USA, Jun. 2015, pp. 3631–3640.
- [15] X. Meng, H. Shen, H. Li, Q. Yuan, H. Zhang, and L. Zhang, "Improving the spatial resolution of hyperspectral image using panchromatic and multispectral images: An integrated method," in *Proc. 7th Workshop Hyperspectral Image Signal Process., Evol. Remote Sens. (WHISPERS)*, Jun. 2015, pp. 1–4.
- [16] F. Palsson, J. R. Sveinsson, M. O. Ulfarsson, and J. A. Benediktsson, "Model-based fusion of multi- and hyperspectral images using PCA and wavelets," *IEEE Trans. Geosci. Remote Sens.*, vol. 53, no. 5, pp. 2652–2663, May 2015.
- [17] M. Parmar, S. Lansel, and B. A. Wandell, "Spatio-spectral reconstruction of the multispectral datacube using sparse recovery," in *Proc. 15th IEEE Int. Conf. Image Process.*, San Diego, CA, USA, Oct. 2008, pp. 473–476.
- [18] B. Arad and O. Ben-Shahar, "Sparse recovery of hyperspectral signal from natural RGB images," in *Proc. Eur. Conf. Comput. Vis. (ECCV)*, Amsterdam, The Netherlands, Oct. 2016, pp. 19–34.
- [19] J. Wu, J. Aeschbacher, and R. Timofte, "In defense of shallow learned spectral reconstruction from RGB images," in *Proc. IEEE Int. Conf. Comput. Vis. Workshops (ICCVW)*, Venice, Italy, Oct. 2017, pp. 471–479.
- [20] R. Timofte, V. De Smet, and L. Van Gool, "A+: Adjusted anchored neighborhood regression for fast super-resolution," in *Proc. Asian Conf. Comput. Vis. (ACCV)*. Cham, Switzerland: Springer, 2014, pp. 111–126.
- [21] N. Akhtar and A. Mian, "Hyperspectral recovery from RGB images using Gaussian processes," *IEEE Trans. Pattern Anal. Mach. Intell.*, vol. 42, no. 1, pp. 100–113, Jan. 2020.
- [22] R. M. H. Nguyen, D. K. Prasad, and M. S. Brown, "Training-based spectral reconstruction from a single RGB image," in *Proc. Eur. Conf. Comput. Vis. (ECCV)*. Cham, Switzerland: Springer, 2014, pp. 186–201.
- [23] L.-C. Chen, G. Papandreou, I. Kokkinos, K. Murphy, and A. L. Yuille, "DeepLab: Semantic image segmentation with deep convolutional nets, Atrous convolution, and fully connected CRFs," *IEEE Trans. Pattern Anal. Mach. Intell.*, vol. 40, no. 4, pp. 834–848, Apr. 2018.
- [24] K. He, X. Zhang, S. Ren, and J. Sun, "Deep residual learning for image recognition," in *Proc. IEEE Conf. Comput. Vis. Pattern Recognit. (CVPR)*, Las Vegas, NV, USA, Jun. 2016, pp. 770–778.
- [25] K. Zhang, W. Zuo, Y. Chen, D. Meng, and L. Zhang, "Beyond a Gaussian denoiser: Residual learning of deep CNN for image denoising," *IEEE Trans. Image Process.*, vol. 26, no. 7, pp. 3142–3155, Jul. 2017.
- [26] Y. Zhang, K. Li, K. Li, L. Wang, B. Zhong, and Y. Fu, "Image super-resolution using very deep residual channel attention networks," in *Proc. Eur. Conf. Comput. Vis. (ECCV)*, Munich, Germany, 2018, pp. 286–301.
- [27] S. Jegou, M. Drozdzal, D. Vazquez, A. Romero, and Y. Bengio, "The one hundred layers tiramisu: Fully convolutional DenseNets for semantic segmentation," in *Proc. IEEE Conf. Comput. Vis. Pattern Recognit. Workshops (CVPRW)*, Honolulu, HI, USA, Jul. 2017, pp. 1175–1183.
- [28] S. Galliani, C. Lanaras, D. Marmanis, E. Baltasavias, and K. Schindler, "Learned spectral super-resolution," 2017, *arXiv:1703.09470*. [Online]. Available: <http://arxiv.org/abs/1703.09470>
- [29] Y. Baran Can and R. Timofte, "An efficient CNN for spectral reconstruction from RGB images," 2018, *arXiv:1804.04647*. [Online]. Available: <http://arxiv.org/abs/1804.04647>
- [30] Z. Shi, C. Chen, Z. Xiong, D. Liu, and F. Wu, "HSCNN+: Advanced CNN-based hyperspectral recovery from RGB images," in *Proc. IEEE/CVF Conf. Comput. Vis. Pattern Recognit. Workshops (CVPRW)*, Salt Lake City, UT, USA, Jun. 2018, pp. 1052–10528.
- [31] U. B. Gewali, S. T. Monteiro, and E. Saber, "Spectral super-resolution with optimized bands," *Remote Sens.*, vol. 11, no. 14, p. 1648, Jul. 2019.
- [32] P. V. Arun, K. M. Buddhiraju, A. Porwal, and J. Chanussot, "CNN based spectral super-resolution of remote sensing images," *Signal Process.*, vol. 169, Apr. 2020, Art. no. 107394.
- [33] K. Zhang, W. Zuo, S. Gu, and L. Zhang, "Learning deep CNN denoiser prior for image restoration," in *Proc. IEEE Conf. Comput. Vis. Pattern Recognit. (CVPR)*, Honolulu, HI, USA, Jul. 2017, pp. 2808–2817.
- [34] W. Dong, P. Wang, W. Yin, G. Shi, F. Wu, and X. Lu, "Denoising prior driven deep neural network for image restoration," *IEEE Trans. Pattern Anal. Mach. Intell.*, vol. 41, no. 10, pp. 2305–2318, Oct. 2019.
- [35] L. Wang, C. Sun, Y. Fu, M. H. Kim, and H. Huang, "Hyperspectral image reconstruction using a deep spatial-spectral prior," in *Proc. IEEE/CVF Conf. Comput. Vis. Pattern Recognit. (CVPR)*, Long Beach, CA, USA, Jun. 2019, pp. 8032–8041.
- [36] Q. Xie, M. Zhou, Q. Zhao, D. Meng, W. Zuo, and Z. Xu, "Multispectral and hyperspectral image fusion by MS/HS fusion net," in *Proc. IEEE/CVF Conf. Comput. Vis. Pattern Recognit. (CVPR)*, Long Beach, CA, USA, Jun. 2019, pp. 1585–1594.
- [37] D. Ren, W. Zuo, D. Zhang, L. Zhang, and M.-H. Yang, "Simultaneous fidelity and regularization learning for image restoration," *IEEE Trans. Pattern Anal. Mach. Intell.*, vol. 43, no. 1, pp. 284–299, Jan. 2021, doi: [10.1109/TPAMI.2019.2926357](https://doi.org/10.1109/TPAMI.2019.2926357).
- [38] M. Simões, J. Bioucas-Dias, L. B. Almeida, and J. Chanussot, "Hyperspectral image superresolution: An edge-preserving convex formulation," in *Proc. IEEE Int. Conf. Image Process. (ICIP)*, Paris, France, Oct. 2014, pp. 4166–4170.
- [39] A. S. Charles and C. J. Rozell, "Spectral superresolution of hyperspectral imagery using reweighted ℓ_1 spatial filtering," *IEEE Geosci. Remote Sens. Lett.*, vol. 11, no. 3, pp. 602–606, Mar. 2014.
- [40] K. Jiang, Z. Wang, P. Yi, G. Wang, T. Lu, and J. Jiang, "Edge-enhanced GAN for remote sensing image superresolution," *IEEE Trans. Geosci. Remote Sens.*, vol. 57, no. 8, pp. 5799–5812, Aug. 2019.
- [41] K. Zhang, W. Zuo, and L. Zhang, "Learning a single convolutional super-resolution network for multiple degradations," in *Proc. IEEE/CVF Conf. Comput. Vis. Pattern Recognit.*, Salt Lake City, UT, USA, Jun. 2018, pp. 3262–3271.
- [42] W. Xie, J. Lei, Y. Cui, Y. Li, and Q. Du, "Hyperspectral pansharpening with deep priors," *IEEE Trans. Neural Netw. Learn. Syst.*, vol. 31, no. 5, pp. 1529–1543, May 2020.
- [43] Q. Zhang, Q. Yuan, J. Li, X. Liu, H. Shen, and L. Zhang, "Hybrid noise removal in hyperspectral imagery with a spatial-spectral gradient network," *IEEE Trans. Geosci. Remote Sens.*, vol. 57, no. 10, pp. 7317–7329, Oct. 2019.
- [44] G. Huang, Z. Liu, L. Van Der Maaten, and K. Q. Weinberger, "Densely connected convolutional networks," in *Proc. IEEE Conf. Comput. Vis. Pattern Recognit. (CVPR)*, Honolulu, HI, USA, Jul. 2017, pp. 2261–2269.
- [45] Y. Wei, Q. Yuan, H. Shen, and L. Zhang, "Boosting the accuracy of multispectral image pansharpening by learning a deep residual network," *IEEE Geosci. Remote Sens. Lett.*, vol. 14, no. 10, pp. 1795–1799, Oct. 2017.
- [46] L. Zhou, Z. Wang, Y. Luo, and Z. Xiong, "Separability and compactness network for image recognition and superresolution," *IEEE Trans. Neural Netw. Learn. Syst.*, vol. 30, no. 11, pp. 3275–3286, Nov. 2019.
- [47] F. Yasuma, T. Mitsunaga, D. Iso, and S. Nayar, "Generalized assorted pixel camera: Post-capture control of resolution, dynamic range and spectrum," Dept. Comput. Sci., Columbia Univ., New York, NY, USA, Tech. Rep. CUCS-061-08, 2008.
- [48] Z. Wang, A. C. Bovik, H. R. Sheikh, and E. P. Simoncelli, "Image quality assessment: From error visibility to structural similarity," *IEEE Trans. Image Process.*, vol. 13, no. 4, pp. 600–612, Apr. 2004.
- [49] F. A. Kruse *et al.*, "The spectral image processing system (SIPS)-interactive visualization and analysis of imaging spectrometer data," *Remote Sens. Environ.*, vol. 44, nos. 2–3, pp. 145–163, 1993.
- [50] D. P. Kingma and J. Ba, "Adam: A method for stochastic optimization," Dec. 2014, *arXiv:1412.6980*. [Online]. Available: <http://arxiv.org/abs/1412.6980>
- [51] L. Biehl and D. Landgrebe, "MultiSpec—A tool for multispectral-hyperspectral image data analysis," *Comput. Geosci.*, vol. 28, no. 10, pp. 1153–1159, Dec. 2002.

- [52] N. Yokoya and A. Iwasaki, "Airborne hyperspectral data over Chikusei," Space Appl. Lab., Univ. Tokyo, Japan, Tech. Rep. SAL-2016-05-27, May 2016.
- [53] Y. Cen *et al.*, "Aerial hyperspectral remote sensing classification dataset of Xiongan New Area (Matiwan Village)," *J. Remote Sens.*, vol. 24, no. 11, pp. 1299–1306, 2019.



Jiang He received the B.S. degree in remote sensing science and technology from the Faculty of Geosciences and Environmental Engineering, Southwest Jiaotong University, Chengdu, China, in 2018. He is currently pursuing the M.S. degree with the School of Geodesy and Geomatics, Wuhan University, Wuhan, China.

His research interests include hyperspectral super-resolution, image fusion, quality improvement, remote sensing image processing, and deep learning.



Jie Li (Member, IEEE) received the B.S. degree in sciences and techniques of remote sensing and the Ph.D. degree in photogrammetry and remote sensing from Wuhan University, Wuhan, China, in 2011 and 2016, respectively.

He is currently an Associate Professor with the School of Geodesy and Geomatics, Wuhan University. His research interests include image quality improvement, image super-resolution reconstruction, data fusion, remote sensing image processing, sparse representation, and deep learning.



Qiangqiang Yuan (Member, IEEE) received the B.S. degree in surveying and mapping engineering and the Ph.D. degree in photogrammetry and remote sensing from Wuhan University, Wuhan, China, in 2006 and 2012, respectively.

In 2012, he joined the School of Geodesy and Geomatics, Wuhan University, where he is currently a Professor. He published more than 90 research articles, including more than 70 peer-reviewed articles in international journals such as the *Remote Sensing of Environment*, *ISPRS Journal of Photogrammetry and Remote Sensing*, *IEEE TRANSACTIONS ON IMAGE PROCESSING*, and *IEEE TRANSACTIONS ON GEOSCIENCE AND REMOTE SENSING*. His current research interests include image reconstruction, remote sensing image processing and application, and data fusion.

Dr. Yuan was a recipient of the Youth Talent Support Program of China in 2019, the Top-Ten Academic Star of Wuhan University in 2011, and the recognition of Best Reviewers of the IEEE GRSL in 2019. In 2014, he received the Hong Kong Scholar Award from the Society of Hong Kong Scholars and the China National Postdoctoral Council. He is also an associate editor of five international journals. He has frequently served as a referee for more than 40 international journals for remote sensing and image processing.



Huanfeng Shen (Senior Member, IEEE) received the B.S. degree in surveying and mapping engineering and the Ph.D. degree in photogrammetry and remote sensing from Wuhan University, Wuhan, China, in 2002 and 2007, respectively.

In 2007, he joined the School of Resource and Environmental Sciences (SRES), Wuhan University, where he is currently a LuoJia Distinguished Professor and the Associate Dean. He was the PI of two projects supported by the National Key Research and Development Program of China and six projects supported by the National Natural Science Foundation of China. He has authored over 100 research articles in peer-reviewed international journals. His research interests include remote sensing image processing, multisource data fusion, and intelligent environmental sensing.

Dr. Shen is a Council Member of the China Association of Remote Sensing Application, an Education Committee Member of the Chinese Society for Geodesy Photogrammetry and Cartography, and a Theory Committee Member of the Chinese Society for Geospatial Information Society. He is also a member of the Editorial Board of *Journal of Applied Remote Sensing* and *Geographical Information Science*.



Liangpei Zhang (Fellow, IEEE) received the B.S. degree in physics from Hunan Normal University, Changsha, China, in 1982, the M.S. degree in optics from the Xi'an Institute of Optics and Precision Mechanics, Chinese Academy of Sciences, Xi'an, China, in 1988, and the Ph.D. degree in photogrammetry and remote sensing from Wuhan University, Wuhan, China, in 1998.

He is currently a "Chang-Jiang Scholar" Chair Professor appointed by the Ministry of Education of China at the State Key Laboratory of Information Engineering in Surveying, Mapping, and Remote Sensing (LIESMARS), Wuhan University. He was a Principal Scientist for the China State Key Basic Research Project from 2011 to 2016 appointed by the Ministry of National Science and Technology of China to lead the Remote Sensing Program in China. He has published more than 700 research articles and five books. He is the Institute for Scientific Information (ISI) Highly Cited Author. He holds 30 patents. His research interests include hyperspectral remote sensing, high-resolution remote sensing, image processing, and artificial intelligence.

Dr. Zhang is a fellow of the Institution of Engineering and Technology (IET). He was a recipient of the 2010 Best Paper Boeing Award, the 2013 Best Paper ERDAS Award from the American Society of Photogrammetry and Remote Sensing (ASPRS), and the 2016 Best Paper Theoretical Innovation Award from the International Society for Optics and Photonics (SPIE). His research teams won the top three prizes of the IEEE GRSS 2014 Data Fusion Contest. His students have been selected as the winners or finalists of the IEEE International Geoscience and Remote Sensing Symposium (IGARSS) Student Paper Contest in recent years. He is also the Founding Chair of the IEEE Geoscience and Remote Sensing Society (GRSS) Wuhan Chapter. He also serves as an associate editor or an editor for more than ten international journals. He is also serving as an Associate Editor for the *IEEE TRANSACTIONS ON GEOSCIENCE AND REMOTE SENSING*.